

Anchoring Drugs to a Zinc(II) Coordination Polymer Network: Exploiting Structural Rationale toward the Design of Metallogels for Drug-Delivery Applications

Protap Biswas and Parthasarathi Dastidar*

Cite This: *Inorg. Chem.* 2021, 60, 3218–3231

Read Online

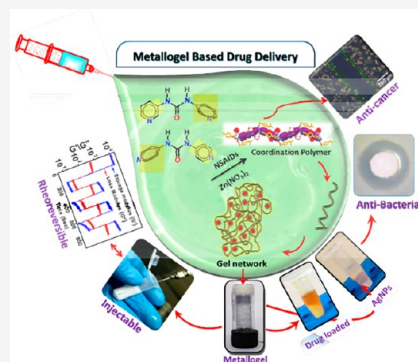
ACCESS |

Metrics & More

Article Recommendations

Supporting Information

ABSTRACT: A new series of coordination polymers (CPs) were synthesized and crystallographically characterized by single-crystal X-ray diffraction with the aim of developing drug-delivery systems via metallogel formation. Structural rationale was employed to design such coordination-polymer-based metallogels. As many as nine CPs were obtained by reacting two bis(pyridyl)urea ligands, namely, 1,3-dipyridin-3-ylurea (3U) and 1,3-dipyridin-4-ylurea (4U), and the sodium salt of various nonsteroidal antiinflammatory drugs, namely, ibuprofen (IBU), naproxen (NAP), fenoprofen (FEN), diclofenac (DIC), meclufenamic acid (MEC), mefenamic acid (MEF), and $\text{Zn}(\text{NO}_3)_2$. All of the CPs displayed 1D polymeric chains that were self-assembled through various hydrogen-bonding interactions involving the urea N–H and carboxylate O atoms and, in a few cases, lattice-occluded water molecules. The reacting components of the CPs produced five metallogels in dimethyl sulfoxide/water. The gels were characterized by rheology and transmission electron microscopy. Three selected metallogelators, namely, 3UMEFg, 3UNAPg, and 3UMECg, showed *in vitro* anticancer, cell imaging, and multidrug delivery for antibacterial applications, respectively. The shear-thinning properties of 3UMECg (rheoreversibility and injectability) make it a potential candidate for plausible topical application.



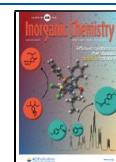
INTRODUCTION

Organic–inorganic hybrid systems (OIHSs), such as porous coordination polymers (PCPs) or metal–organic frameworks (MOFs), are emerging materials for various applications¹ including drug-delivery systems (DDSs).^{2–10} Delivering an active pharmaceutical ingredient (API) or drug to the target site is a challenging task. It requires the development of a vehicle that protects the API/drug from being destroyed by the immune response of the subject. There have been a number of various organic^{11–15} and inorganic^{16–20} systems developed as vehicles for drug delivery purposes. However, hybrid systems like OIHSs as drug-delivery vehicles offer quite a few advantages over vehicles developed from purely organic or inorganic compounds; they (a) are relatively easily synthesized because of the less energy expensive metal–ligand coordination bond compared to the covalent bond, (b) are often highly crystalline, allowing access to atomic-level structural information by single-crystal X-ray diffraction (SXRD), crucial for fine-tuning, (c) have tunable physicochemical properties arising from virtually infinite combinations of ligands and metal salts, and (d) have a relatively labile metal–ligand coordination bond compared to the covalent bond, facilitating postapplication degradation. PCPs such as MIL-100 and MIL-101 were exploited by Férey et al. for the first time as vehicles for the controlled release of nonsteroidal antiinflammatory drugs (NSAIDs), namely, Ibuprofen.²¹ Since then, there have been

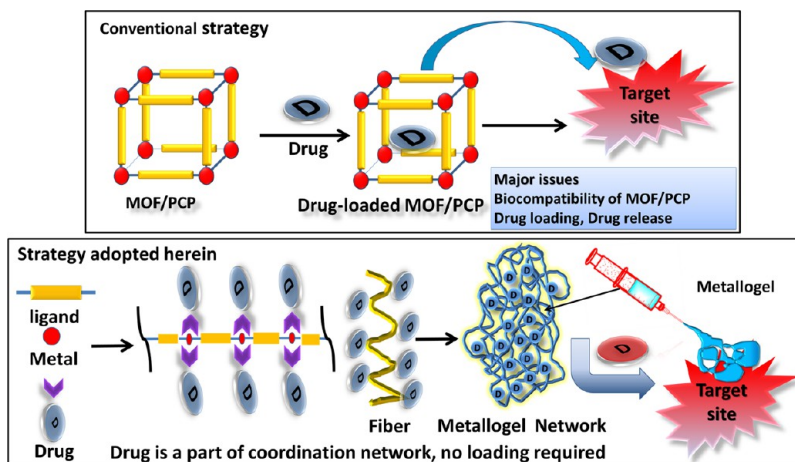
many reports on PCP-based DDSs.^{22–26} Various parameters such as absorption, distribution, metabolism, excretion, and toxicity (ADMET), which are important for developing DDSs, could be fine-tuned in such OIHSs.^{27,28} Nevertheless, OIHSs as drug-delivery vehicles possess a number of disadvantages: loading of the API/drug into the pores requires compatibility of the size and chemical environment of the active ingredient with that of the pores of the PCPs or MOFs, and subsequent release of the API/drug in a controlled fashion is often found to be difficult. To overcome such challenges associated with the use of vehicles for drug delivery, an alternative concept, namely, “self-delivery” (without involving any vehicle), is being developed.^{29,30} Among the various approaches to achieving such goals, supramolecular gelation^{31–37} is found to be quite promising; in this approach, the API/drug under study is converted to a supramolecular gelator by following certain design strategies, and the resulting gel can then be administered to the target site via either a topical (noninvasive) or a subcutaneous (invasive) route.^{38–44,70–72}

Received: December 4, 2020

Published: February 11, 2021



Scheme 1. OIHS-Based Drug-Delivery Strategies



Because the gel is made from a modified API/drug, there is no need for a vehicle; the API/drug-based gel itself is delivered to the target site, hence the name “self-delivery”.

In the context of developing OIHS-based DDSs, one can make the API/drug part of the coordination framework in such a manner that the resulting coordination compound produces a metallogel, which can then be administered for such biomedical applications. With the API/drug being stoichiometric, the difficulty of drug loading does not exist. On the other hand, a strong and labile coordination bond may facilitate the slow release of the API/drug from the gel (Scheme 1). This approach, although quite appealing, is not highly explored.^{45,46}

Herein, we report a new series of metallogels derived from rationally designed and crystallographically characterized coordination polymers (CPs), which were synthesized by reacting two bidentate bis(pyridyl)bis(urea) ligands, namely, 1,3-dipyridin-3-ylurea (**3U**), 1,3-dipyridin-4-ylurea (**4U**), and sodium salts of various NSAIDs and $\text{Zn}(\text{NO}_3)_2$. As envisaged (vide supra), some of the reactants of the CPs produced metallogels (Scheme 2). Three selected metallogelators (**3UMEF**, **3UNAP**, and **3UMEC**) were further evaluated for drug-delivery applications. Most likely, the CP-based metal-

logels for drug-delivery applications reported herein were hitherto unknown.

EXPERIMENTAL SECTION

Materials and Methods. All of the chemicals and solvents were commercially available and were used without further purification. NMR spectra were recorded using a 400 MHz/500 MHz spectrometer (Bruker Ultrashield Plus-400/500). SXRD data were collected in a Bruker APEX II diffractometer equipped with a CCD area detector. Powder X-ray diffraction (PXRD) data were recorded on a Bruker AXS D8 Advance (Cu $K\alpha$ radiation, $\lambda = 1.5406 \text{ \AA}$) powder X-ray diffractometer. Fourier transform infrared (FT-IR) spectra were recorded on a PerkinElmer FT-IR spectrometer. UV–vis spectroscopic measurements were carried out on a Hewlett-Packard 8453 diode-array spectrophotometer. The elemental compositions of the purified compounds were confirmed by elemental analysis (PerkinElmer Precisely, Series-II, CHNO/S Analyzer-2400). Transmission electron microscopy (TEM) images were recorded using a JEOL (JEM 2100F) instrument on 300 mesh copper TEM grid. Matrix-assisted laser desorption/ionization time-of-flight mass spectrometry (MALDI-TOF MS) spectra were collected in a Bruker instrument with a DHB matrix. Images were analyzed using *ImageJ* software. 3-(4,5-Dimethylthiazol-2-yl)-2,5-diphenyltetrazolium bromide (MTT) assay plate scanning was conducted using a multiplate ELISA reader (Varioskan Flash Elisa Reader, Thermo Fisher). Fluorescence images were collected by laser scanning confocal microscopy (LSCM; Carl Zeiss). Rheological experiments were performed with an Anton Paar MCR 102 modular compact rheometer.

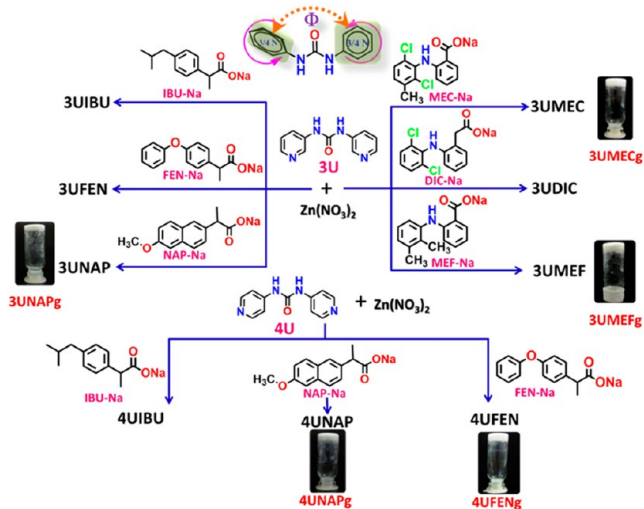
The bis(pyridyl)urea ligands (**3U** and **4U**) were synthesized following the reported literature.^{73,74} The detailed synthetic procedure is described in the [Supporting Information](#).

Characterization Data of the Ligands. **3U.** Yield: 900 mg, 66.25%. ^1H NMR (500 MHz, $\text{DMSO-}d_6$): δ 8.96 (s, 1H), 8.59 (s, 1H), 8.19 (d, $J = 4.6 \text{ Hz}$, 1H), 7.92 (d, $J = 8.3 \text{ Hz}$, 1H), 7.30 (dd, $J = 8.2$ and 4.7 Hz , 1H) (Figure S1). ^{13}C NMR (125 MHz, $\text{DMSO-}d_6$): δ 153.2, 143.6, 140.8, 136.6, 125.9, 124.1 (Figure S2). FT-IR (cm^{-1}): $\tilde{\nu}$ 3045 (brs, urea N–H stretch), 1690 (s, urea C=O stretch) (Figure S3). MALDI-TOF MS (DHB matrix/MeOH). Calcd for $[\text{M} + \text{H}]^+$: m/z 215.23. Found: m/z 215.25 (Figure S4).

4U. Yield: 960 mg, 69.75%. ^1H NMR (500 MHz, $\text{DMSO-}d_6$): δ 9.27 (1 H, s), 8.38 (2 H, d, $J = 5.4 \text{ Hz}$), 7.44 (2 H, d, $J = 5.6 \text{ Hz}$) (Figure S5). ^{13}C NMR (125 MHz, $\text{DMSO-}d_6$): δ 151.7, 150.2, 145.9, 112.4 (Figure S6). FT-IR (cm^{-1}): $\tilde{\nu}$ 3004 (brs, urea N–H stretch), 1739 (s, urea C=O stretch) (Figure S7). MALDI-TOF MS (DHB matrix/MeOH). Calcd for $[\text{M} + \text{H}]^+$: m/z 215.23. Found: m/z 215.26 (Figure S8).

Synthesis of CPs and Characterization Data. The CPs were synthesized by a crystallization method. The sodium salt of the

Scheme 2. CPs and Metallogels Reported in This Study



corresponding NSAID (1 equiv, 0.1 mmol) was dissolved in water (4 mL) and placed in crystallization test tube (15 cm height and 1 cm diameter). 3U or 4U (0.5 equiv, 0.05 mmol) was dissolved in methanol (MeOH; 4 mL) and poured slowly over the aqueous solution of NSAIDs. Finally, a metal salt [$\text{Zn}(\text{NO}_3)_2 \cdot 6\text{H}_2\text{O}$, 0.5 equiv, 0.05 mmol] solution in ethanol (2 mL) was layered over the reaction mixture. Typically, after 3 weeks, crystals had grown at the interface of the water/MeOH layer. The crystals were collected by a paint brush, washed with MeOH, and dried on filter paper under ambient conditions.

Characterization Data of the CPs. 3UIBU. FT-IR (cm^{-1}): $\tilde{\nu}$ 3256, 3091, 2954, 1717, 1588, 1488, 1428, 1358, 1277, 1209, 1134, 1068, 912, 807, 696, 647, 542 (Figure S9). CHN anal. Calcd (expt): C, 64.39 (64.26); H, 6.43 (6.78); N, 8.12 (8.21).

3UNAP. FT-IR (cm^{-1}): $\tilde{\nu}$ 3220, 2932, 1703, 1605, 1558, 1485, 1391, 1255, 1211, 1161, 1032, 926, 796, 750, 700, 647, 521, 471 (Figure S10). CHN anal. Calcd (expt): C, 61.95 (61.68); H, 5.07 (4.96); N, 7.41 (7.41).

3UFEN. FT-IR (cm^{-1}): $\tilde{\nu}$ 3281, 3064, 1710, 1580, 1557, 1484, 1385, 1355, 1256, 1207, 1059, 929, 881, 763, 763, 692, 651, 484, 455 (Figure S11). CHN anal. Calcd (expt): C, 64.61 (64.85); H, 4.76 (4.47); N, 6.73 (6.67).

3UDIC. FT-IR (cm^{-1}): $\tilde{\nu}$ 3283, 3087, 1703, 1631, 1489, 1454, 1270, 1207, 745, 710, 692, 564, 534 (Figure S12). CHN anal. Calcd (expt): C, 53.84 (53.85); H, 3.48 (3.10); N, 9.66 (9.10).

3UMEC. FT-IR (cm^{-1}): $\tilde{\nu}$ 3270, 3061, 1716, 1609, 1548, 1495, 1414, 1287, 1197, 1089, 1039, 806, 752, 695, 653, 604, 463 (Figure S13). CHN anal. Calcd (Expt): C, 53.85 (53.55); H, 3.49 (3.48); N, 9.69 (9.69).

3UMEF. FT-IR (cm^{-1}): $\tilde{\nu}$ 3280, 3065, 1709, 1609, 1578, 1548, 1489, 1387, 1284, 1202, 1151, 1062, 783, 693, 653, 615, 470 (Figure S14). CHN anal. Calcd (Expt): C, 64.61 (64.61); H, 4.76 (4.54); N, 6.76 (7.06).

4UIBU. FT-IR (cm^{-1}): $\tilde{\nu}$ 3262, 2957, 1739, 1585, 1505, 1435, 1335, 1288, 1190, 1066, 1025, 838, 734, 534 (Figure S15). CHN anal. Calcd (Expt): C, 62.75 (62.82); H, 6.50 (6.55); N, 7.71 (7.88).

4UNAP. FT-IR (cm^{-1}): $\tilde{\nu}$ 3272, 2964, 1746, 1588, 1513, 1439, 1293, 1179, 1067, 1031, 849, 830, 732, 664, 532, 478 (Figure S16). CHN anal. Calcd (expt): C, 63.6 (63.98); H, 4.65 (4.69); N, 7.61 (7.50).

4UFEN. FT-IR (cm^{-1}): $\tilde{\nu}$ 3278, 3078, 1744, 1576, 1490, 1437, 1395, 1249, 1191, 1066, 839, 762, 692, 603, 535 (Figure S17). CHN anal. Calcd (expt): C, 64.61 (64.86); H, 4.76 (4.97); N, 7.73 (7.65).

SXRD. Intensity data of X-ray diffraction were collected on a Bruker SMART APEX-II diffractometer (Mo $K\alpha$, $\lambda = 0.7107 \text{ \AA}$) equipped with a CCD area detector. The data reduction, structure solution, and refinement were carried out using the APEX-3 SMART software package. All of the structures were solved by direct methods and refined by full-matrix least squares based on F^2 against all reflections in the SHELXL-2014⁴⁷ suite of APEX-3. The final refinement, disorder treatment, and CIF finalization were carried out in OLEX2, version 1.2.8.⁴⁸ 3UMEC was found to be nonmerohedrally twinned, with a twin fraction of 0.540(3) that was solved by separating two domains in the reciprocal lattice; data scaling was carried out using TWINABS program, and structure refinement was carried out with the HKLF5 file in SHELXL in APEX-3. The methyl C atom in the ibuprofen molecule of 3UIBU and the methyl C atoms in both meclofenamate moieties in 3UMEC were disordered over two positions with refined SOFs of 0.259(7)/0.741(7), 0.46(2)/0.54(2), and 0.512(13)/0.488(13), respectively. The methoxy group of 3UNAP was disordered over two positions with a refined SOF of 0.568(14)/0.432(14). The methyl and isopropyl groups of 4UIBU were also disordered over two positions with a refined SOF of 0.354(10)/0.646(10). All of the non-H atoms were anisotropically refined. The H atoms connected to the heteroatoms or hydrogen-bonded H atoms were located on the difference Fourier maps and refined; in the other cases, they were fixed wherever possible. Crystallographic data for the structural analysis of compounds reported herein have been deposited at the Cambridge Crystallographic Data Centre as CCDC 1878233–1878241.

PXRD. PXRD data were recorded using a Bruker AXS D8 Advance (Cu $K\alpha$ radiation, $\lambda = 1.5406 \text{ \AA}$) powder diffractometer equipped with a superspeed LYNXEYE detector. Finely powdered samples ($\sim 20 \text{ mg}$) were placed over a glass slide to collect data. The experiments were carried out at 40 kV and 40 mA with a scan speed of 0.2 s/step (step size = 0.02°) for a scan range of $5\text{--}35^\circ$ (2θ). The PXRD data for silver nanoparticles (AgNPs) with the gel were collected with Rigaku Smartlab (40 kV, 110 mA, Cu $K\alpha_1$ radiation, $\lambda = 1.5406 \text{ \AA}$, step size = 0.010). Simulated PXRD patterns were generated from the CIFs using Mercury 3.8 software.

TEM. In a typical experiment, the metallogel sample was smeared on a carbon-coated copper grid (300 mesh) and dried at room temperature for 24 h (except for 4UMEFg, which was dried in a vacuum desiccator at room temperature), and the TEM images were recorded at an accelerating voltage of 200 kV without any staining.

Rheology. Parallel-plate geometry (25 mm diameter with a 1 mm gap) was employed to collect rheological data on freshly prepared dimethyl sulfoxide (DMSO)/water (1:1, v/v) metallogels (10 wt %, w/v). The frequency sweep data (G' and G'' vs frequency ω , rad/s) were collected at a fixed strain guided by the linear viscoelastic (LVE) region obtained from an amplitude sweep (G' and G'' vs strain). The thixotropic data were collected using strains of 65% (higher than the critical strain) and 1% with a relaxation time of 120 s for three consecutive cycles.

Loading and Release of Sulfasalazine (SUL). The metallogel 3UMECg (1 mL, 10 wt %; DMSO/water, 1:1, v/v) was taken in a vial. A solution of SUL (1 mL, 1 mg/mL; 1:1 DMSO/water) was prepared and placed over the metallogel bed to diffuse the drug (SUL) into the metallogel, and photographs were taken at various time intervals. The loading efficiency was determined by UV-vis using a supernatant (10 μL). After complete absorption of SUL, as revealed from the UV-vis data, the supernatant was replaced with phosphate-buffered saline (PBS; 1 mL, 7.2 pH) to monitor the release of SUL, which could be qualitatively observed by the yellow coloration of the supernatant and quantitatively determined by UV-vis using 10 μL aliquots at various time intervals.

AgNP Generation in the Metallogel. A silver nitrate (AgNO_3) solution (1 mL, 1 mg/mL; 1:1 DMSO/water) was placed over 3UMECg (1 mL, 10 wt %) taken in a vial and kept at room temperature under laboratory light for 24 h. A UV-vis spectrum of the AgNP-containing metallogel was recorded by dispersing it in DMSO.

MTT Assay. The cells (B16F10) were purchased from the National Centre for Cell Science (Pune, India) and cultured in a high-glucose Dulbecco's modified Eagle's medium (DMEM) containing 10% fetal bovine serum and 1% penicillin/streptomycin in a humidified incubator at 37°C under a 5% CO_2 atmosphere until its confluence. The cells were then seeded in a 96-well plate at a density of $\sim 10^4$ cells/well. The culture plates were then incubated for 24 h in a humidified incubator at 37°C under a 5% CO_2 atmosphere. Primary stock solutions of the CPs were prepared by dispersing the corresponding CPs (20 mg) in cell-culture-grade DMSO (1 mL). The stock solutions were further diluted with DMEM (40–160 $\mu\text{g}/\text{mL}$); 150 μL of DMEM containing the CPs was then added to the well and incubated at 37°C under a 5% CO_2 atmosphere for 72 h. The culture medium of each well plate was replaced with a MTT reagent (100 μL , 0.5 mg/mL, in DMEM) and incubated further for 3 h. The culture medium was discarded and replenished with 100 μL of DMSO. The well plate was then read under a multiplate ELISA reader ($\lambda = 570 \text{ nm}$) to measure the intensity of formazan, which was attributed to the live cell concentration. The percentage of live cells under treatment with the CPs was calculated by considering the DMEM-treated cells (control) to be 100%. All of the experiments were performed three times.

Cell Migration. The cells were cultured and seeded in a 35 mm 6-well plate and incubated until its confluence. A uniform scratch line was drawn by a sterile pipet microtip in the middle of the well plate. The CP 3UMEF (1 mL in DMEM at $\text{IC}_{50} \sim 80 \mu\text{g}/\text{mL}$) was added to the well plate. For control experiments, only DMEM, free drug (MEFH), and 3U were added to the well plate. The amounts of

Table 1. Crystallographic Table

	3UIBU	3UFEN	3UNAP	3UMEC	3UMEF	3UDIC	4UIBU	4UFEN	4UNAP
CCDC	1878237	1878236	1878240	1878233	1878241	1878234	1878238	1878235	1878239
empirical formula	C ₃₇ H ₄₀ N ₄ O ₃ Zn	C ₄₁ H ₃₆ N ₄ O ₃ Zn	C ₃₉ H ₃₇ N ₄ O ₃ Zn	C ₃₉ H ₃₈ Cl ₄ N ₄ O ₃ Zn	C ₄₁ H ₃₈ N ₄ O ₃ Zn	C ₃₉ H ₃₈ Cl ₄ N ₄ O ₃ Zn	C ₃₇ H ₄₀ N ₄ O ₃ Zn	C ₄₁ H ₃₈ N ₄ O ₃ Zn	C ₃₉ H ₃₆ N ₄ O ₃ Zn
fw/(g/mol)	690.13	762.11	755.09	867.84	760.14	869.86	708.15	780.12	738.09
temp/K	120	120(2)	298.92	150.15	120	296.15	296.15	296.15	100.09
cryst syst	monoclinic	monoclinic	monoclinic	triclinic	triclinic	monoclinic	monoclinic	monoclinic	monoclinic
space group	P2 ₁ /c	P2 ₁ /c	P2 ₁	P $\bar{1}$	P $\bar{1}$	P2 ₁ /c	P2 ₁ /n	P2 ₁ /n	P2 ₁
a/Å	17.2328(8)	16.7082(16)	11.833(2)	12.2884(11)	11.454(11)	16.2474(2)	9.3310(17)	9.4929(8)	10.1514(7)
b/Å	12.2234(5)	10.9947(10)	12.6847(19)	12.4340(10)	12.420(12)	14.2063(2)	22.810(4)	23.527(2)	33.568(2)
c/Å	17.5064(8)	20.1742(19)	24.418(4)	14.0236(13)	13.945(13)	16.7078(2)	17.316(3)	16.946(2)	10.1553(7)
α /deg	90	106.831(2)	90	92.601(3)	95.373(13)	90	90	90	90
β /deg	90	107.760(5)	90.498(11)	115.523(3)	114.209(13)	102.5070(10)	91.673(3)	90.535(6)	93.963(2)
γ /deg	90	90	90	92.673(3)	93.790(14)	90	90	90	90
volume/Å ³	3529.6(3)	3529.4(6)	3665.0(10)	1926.4(3)	1790(3)	3764.90(8)	3684.1(12)	3784.7(6)	3452.3(4)
Z	4	4	4	2	2	4	4	4	4
$\rho_{\text{calc}}/(\text{g cm}^{-3})$	1.299	1.434	1.368	1.496	1.411	1.535	1.277	1.369	1.42
μ/mm^{-1}	0.743	0.755	0.728	0.967	0.742	0.99	0.715	0.707	0.769
F(000)	1456	1584	1572	884	792	1776	1496	1624	1536
cryst size/mm ³	0.23 × 0.21 × 0.2	0.3 × 0.3 × 0.1	0.35 × 0.21 × 0.1	0.23 × 0.21 × 0.2	0.45 × 0.12 × 0.1	0.23 × 0.21 × 0.15	0.21 × 0.2 × 0.15	0.3 × 0.25 × 0.2	0.23 × 0.12 × 0.1
radiation	Mo K α (λ = 0.71073)	Mo K α (λ = 0.71073)	Mo K α (λ = 0.71073)	Mo K α (λ = 0.71073)	Mo K α (λ = 0.71073)	Mo K α (λ = 0.71073)			
2 θ range for data collection/deg	2.468–54.466	2.56–51.032	3.336–50.696	4.754–57.424	3.316–42.224	2.568–60.518	2.954–50.674	3.462–50.714	4.2–53.48
index ranges	–22 ≤ h ≤ 22, –15 ≤ k ≤ 15, –22 ≤ l ≤ 22	–19 ≤ h ≤ 20, –13 ≤ k ≤ 13, –24 ≤ l ≤ 24	–14 ≤ h ≤ 13, –15 ≤ k ≤ 15, –29 ≤ l ≤ 29	–16 ≤ h ≤ 14, –16 ≤ k ≤ 16, 0 ≤ l ≤ 18	–11 ≤ h ≤ 11, –12 ≤ k ≤ 12, –14 ≤ l ≤ 14	–22 ≤ h ≤ 23, –20 ≤ k ≤ 20, –22 ≤ l ≤ 23	–11 ≤ h ≤ 11, –27 ≤ k ≤ 27, –20 ≤ l ≤ 20	–11 ≤ h ≤ 11, –17 ≤ k ≤ 28, –16 ≤ l ≤ 20	–12 ≤ h ≤ 12, –39 ≤ k ≤ 42, –12 ≤ l ≤ 12
reflins collected	75404	37978	56828	9328	14594	87726	89861	15867	39602
indep reflns	7837 [R _{int} = 0.0451, R _σ = 0.0286]	6523 [R _{int} = 0.0568, R _σ = 0.0418]	13403 [R _{int} = 0.0831, R _σ = 0.0867]	9328 [R _{int} = ?, R _σ = 0.1770]	3865 [R _{int} = 0.1477, R _σ = 0.1413]	11037 [R _{int} = 0.0548, R _σ = 0.0388]	6728 [R _{int} = 0.0670, R _σ = 0.0307]	6844 [R _{int} = 0.0399, R _σ = 0.0659]	13867 [R _{int} = 0.1029, R _σ = 0.1125]
data/restraints/param	7837/1/435	6523/0/482	13403/19/944	9328/0/509	3865/0/470	11037/0/512	6728/1/482	6844/1/482	13867/1/921
GOF on F ²	1.097	1.043	1.003	1.028	0.989	1.009	1.01	1.044	1.021
final R indexes [I ≥ 2 σ (I)]	R ₁ = 0.0503, wR ₂ = 0.1325	R ₁ = 0.0556, wR ₂ = 0.1216	R ₁ = 0.0541, wR ₂ = 0.1160	R ₁ = 0.0944, wR ₂ = 0.2205	R ₁ = 0.0591, wR ₂ = 0.1212	R ₁ = 0.0345, wR ₂ = 0.0677	R ₁ = 0.0528, wR ₂ = 0.1285	R ₁ = 0.0751, wR ₂ = 0.1750	R ₁ = 0.0660, wR ₂ = 0.1517
largest diff peak/hole/(e/Å ³)	1.75/–0.66	1.26/–0.92	0.64/–0.57	1.04/–0.95	0.45/–0.51	0.42/–0.55	0.87/–0.47	1.35/–1.30	1.42/–0.76

MEFH and 3U added were equivalent to that present in 3UMEF at its IC_{50} concentration. The well plate was then incubated for 24 h, and during this incubation period, still images were captured under an optical microscope (Olympus CKX31) at different time intervals in order to measure the migration speed.

Cell Imaging. The cells were cultured in a 35 mm confocal dish and incubated overnight in a humidified incubator at 37 °C under a 5% CO_2 atmosphere. After 24 h, when the cells were adhered to the dish, the old medium was discarded and the cells were washed with PBS (pH 7.4). 3UNAP (2 mL in DMEM at $IC_{50} = 80 \mu\text{g/mL}$) was added to the dish and incubated for 20 min at 37 °C under a 5% CO_2 atmosphere. The medium was then sucked out, the dish was washed several times with PBS (pH 7.4) to remove the unbound drugs, and then the cells were further treated with 4% paraformaldehyde and kept for 15 min in the dark for cell fixation. 4',6-Diamidino-2-phenylindole (DAPI) was used for staining the nucleus. For this purpose, a DAPI/PBS solution (2 mL, 5 nM) was added to the cells, followed by incubation for 5 min. Extracellular staining was removed by washing the cells with PBS (pH 7.4). After fresh PBS (1 mL, pH 7.4) was added to the cells, images were recorded by using a Carl Zeiss laser scanning confocal microscope.

Antibacterial Zone Assay. *Klebsiella* spp. was grown from single-colony isolation in liquid broth media supplemented with peptone, yeast extract, and NaCl. For zone assay, the bacteria (100 μL in broth media) were spread uniformly on an agar-gel plate (1.5 wt % containing the above-mentioned supplements). Grooves (1 cm) were cut and filled with 100 μL of 3UMECg, AgNP@3UMECg, SUL@3UMECg, and nothing (control). Then the plate was incubated at 37 °C for 24 h in an incubator, and a digital photograph was taken.

RESULTS AND DISCUSSION

Design and Synthesis of the Metallogelators. Because of the lack of adequate molecular-level information behind gelation, designing a gelator, be it organic or metal–organic, is a formidable task.^{49–52} Since the first report of metallogelation displayed by calixarene-based CPs,⁵³ there have been efforts to bring in some rationale to design metallogelators; for example, we and others have proposed that molecular systems that encourage strong interactions with solvents through various supramolecular interactions resulting in lattice-occluded crystalline solids (LOCSs) are potential targets as gelators because large amounts of solvent molecules are trapped in both gels and LOCSs.^{54,55}

Thus, to design CP-based metallogelators, we chose two bidentate ligands having a urea backbone, namely, 1,3-dipyridin-3-ylurea (3U) and 1,4-dipyridin-3-ylurea (4U), that would form 1D CPs^{75–80} when reacted with $Zn(NO_3)_2$ and various NSAIDs (ibuprofen or IBU, naproxen or NAP, fenoprofen or FEN, diclofenac or DIC, meclofenamic acid or MEC, and mefenamic acid or MEF) in their carboxylate form (sodium salt); the drug molecules are expected to remain anchored to the 1D coordination network, thereby making the drug molecule a part of the coordination network as envisaged. Possibilities of interchain assembly and entrapment of solvent molecules because of the excellent hydrogen-bonding capability of the urea backbone make the OIHS suitable for producing metallogels. As many as nine CPs were isolated as single crystals from the reactions (see Scheme 2, Table 1, and the Experimental Section). It may be noted that the reaction of 4U and $Zn(NO_3)_2$ with MEC, DIC, and MEF did not produce any single crystals; instead, relatively poorly diffracting microcrystals were obtained (Figure S46).

SXRD. *Crystal Structure of 3UIBU.* The space group of 3UIBU was determined to be the centrosymmetric monoclinic $P2_1/c$. The asymmetric unit contained one Zn(II) metal center coordinated by two IBU and one 3U ligands through

carboxylate O and pyridyl N atoms, respectively; while the carboxylate of one of the IBU ligands displayed unidentate coordination, the other one coordinated to the metal center through a bidentate mode; the metal center Zn(II) showed five-coordinated highly distorted trigonal-bipyramidal geometry wherein the equatorial positions were occupied by two carboxylate O atoms from two IBU ligands and one pyridyl N atom and the axial positions were coordinated by one pyridyl N and one carboxylate O atoms; such five-coordinated coordination geometry of Zn(II) was because of the bidentate coordination mode of one of the carboxylates. The methyl group in one of the IBU ligands was found to be disordered over two positions (see the Experimental Section). Crystal structure analysis revealed that the bis(pyridyl)urea ligand 3U was highly nonplanar, displaying a dihedral angle (Φ) of $\sim 63^\circ$ involving the planes of the terminal pyridyl rings; overall, 3UIBU was an 1D zigzag CP formed because of the extended coordination of the bidentate ligand 3U, and the drug molecules IBU were found to be anchored to the Zn(II) centers as envisaged. The 1D chains were found to self-assemble into a 2D hydrogen-bonded network sustained by N–H \cdots O hydrogen-bonding interactions involving one of the N atoms of the urea moiety and the IBU carboxylate O atom, which was free from coordination. Such 2D hydrogen-bonded networks were further packed in a parallel fashion sustained by dispersion forces (Figure 1).

Crystal Structure of 3UFEN. Crystallized in the centrosymmetric monoclinic space group $P2_1/c$, the asymmetric unit of 3UFEN comprised one 3U ligand, two FEN ligands, and one Zn(II) metal center; both FEN molecules displayed a

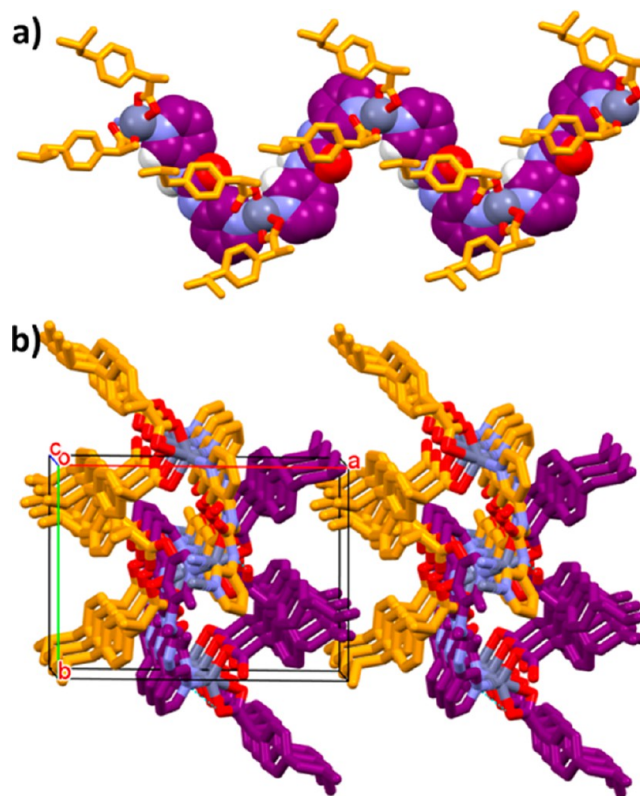


Figure 1. Crystal structure illustration of 3UIBU: (a) 1D CP chain with the anchored drug molecule IBU and (b) packing of the hydrogen-bonded 1D CP chains viewed down the c axis.

unidentate coordination mode to Zn(II), and 3U remained coordinated to the metal center by a pyridyl N atom. The bis(pyridyl)urea ligand 3U displayed near-planar conformation with dihedral angle $\Phi = \sim 14^\circ$. Because of the extended coordination involving the ligand 3U with Zn(II), a 1D zigzag CP chain was formed wherein the drug component remained anchored. The usual urea synthon was not observed in the structure; instead, one of the urea N–H atoms was involved in N–H \cdots O interactions with the carboxylate O atom of the neighboring chain, resulting in parallel packing of the chains and producing a 2D hydrogen-bonded network that further packed in a parallel fashion stabilized by dispersion forces (Figure 2).

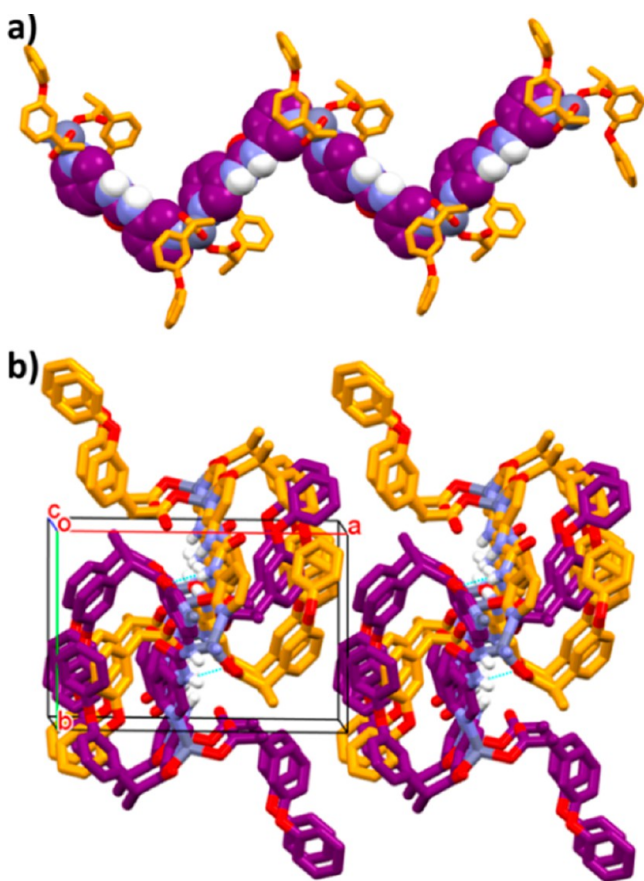


Figure 2. Crystal structure illustration of 3UFEN: (a) 1D CP chain with the anchored drug molecule FEN and (b) packing of the hydrogen-bonded 1D CP chains viewed down the *c* axis.

Crystal Structure of 3UNAP. The crystal structure belonged to the noncentric monoclinic space group $P2_1$. The asymmetric unit comprised two crystallographically independent moieties, each one containing one Zn(II) atom, one 3U ligand, two NAP ligands, and two molecules of lattice-occluded water. The coordinating modes of the NAP units to the metal centers were different in two moieties; in one moiety, the NAP molecules were coordinated to the Zn(II) atom via a unidentate mode, whereas in the other moiety, it displayed both unidentate and bidentate coordination modes. The methoxy group of NAP in one of the crystallographically independent moieties was found to be disordered over two positions (see the Experimental Section). The bidentate ligand 3U displayed a significantly nonplanar conformation with $\Phi =$

~ 45 and 48° in two independent moieties, and the Zn(II) atom showed distorted tetrahedron geometry in one moiety, whereas it was a five-coordinated species in the other because of the bidentate coordination mode of the carboxylate. Both of the independent moieties formed 1D polymeric chains because of the extended coordination involving the pyridyl N atoms of the bidentate ligand 3U. Each crystallographically independent 1D chain self-assembled with itself via hydrogen-bonding interactions of the type N–H \cdots O involving the urea N–H and carboxylate O atoms. The lattice-occluded water molecules were located within the interstitial space via O–H \cdots O hydrogen bonding with the carboxylate O atoms. All of the chains were packed in a parallel fashion (Figure 3).

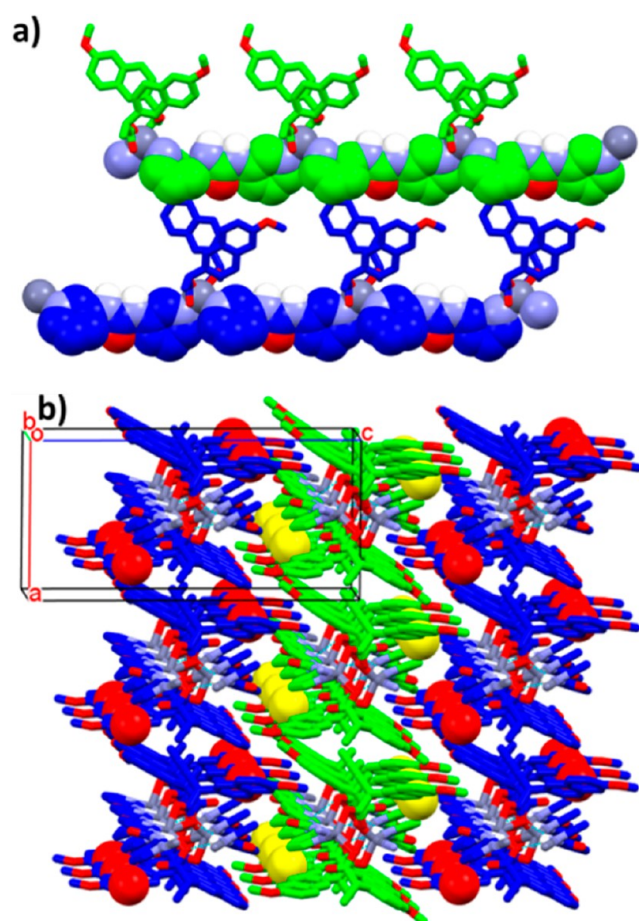


Figure 3. Crystal structure illustration of 3UNAP: (a) two crystallographically independent 1D CP chains (shown in different colors) with the anchored drug molecule NAP and (b) packing of the hydrogen-bonded dimer of the 1D CP chains with lattice-occluded water molecules (shown in the space-filling model) viewed down the *b* axis.

Crystal Structure of 3UDIC. The centrosymmetric monoclinic space group $P2_1/c$ was assigned to 3UDIC. In the asymmetric unit, one Zn(II) metal ion was found to be coordinated by two DIC ligands via carboxylate Zn coordination in a unidentate mode and one 3U ligand via a pyridyl N atom; the contents of the asymmetric unit were in general positions. Because of the extended coordination involving the bis(pyridyl)urea ligand 3U and Zn(II), the supramolecular architecture of 3UDIC may be best described as a 1D zigzag polymer wherein the drug molecules DIC were

anchored to the metal centers. The coordination geometry of Zn(II) was distorted octahedral, wherein two sites were occupied by the pyridyl N atoms of 3U and the other two positions were coordinated by carboxylate O atoms of DIC. The urea ligand displayed a highly nonplanar conformation with $\Phi = \sim 59^\circ$. 1D CP chains self-assembled to form 2D hydrogen-bonded networks via N–H \cdots O interactions involving the urea N–H and carboxylate O atoms of the interacting chains. Such an assembly further packed in a parallel fashion stabilized by dispersion forces (Figure 4).

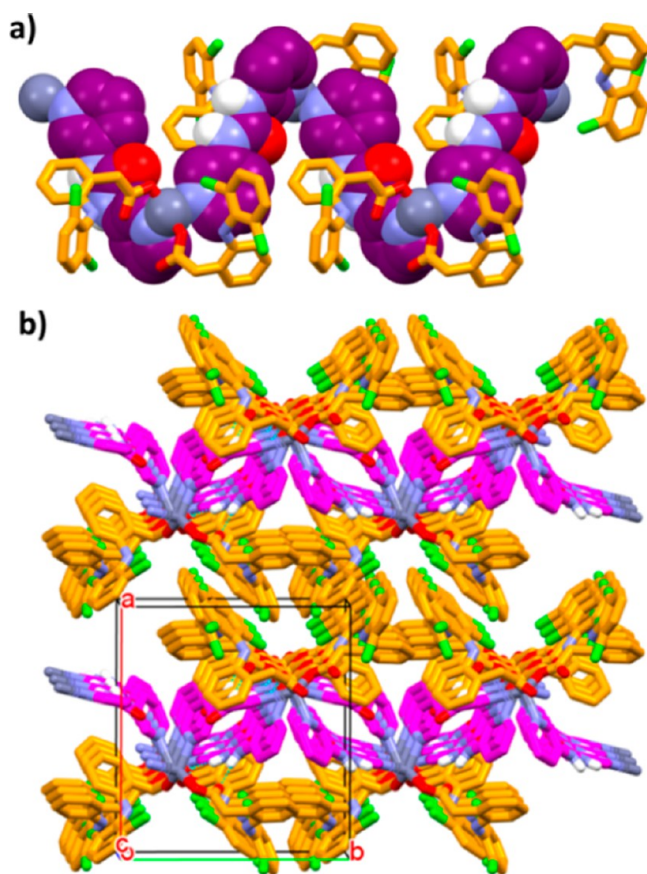


Figure 4. Crystal structure illustration of 3UDIC: (a) 1D CP chains with the anchored drug molecule DIC and (b) packing of the hydrogen-bonded dimer of the 1D CP chains viewed down the *c* axis.

Crystal Structure of 3UMEC. The refined model of 3UMEC belonged to the centrosymmetric triclinic space group $P\bar{1}$. The asymmetric unit contained one Zn(II) atom coordinated by one 3U ligand by one pyridyl N and two MEC atoms via carboxylate O atoms displaying unidentate coordination, all located on general positions. The dichloromethylbenzene rings of both of the crystallographically independent drug moieties were rotationally disordered because of C–N bond rotation (see the Experimental Section). While the metal center showed distorted tetrahedral geometry, the bidentate bis(pyridyl)urea ligand displayed a nonplanar conformation with $\Phi = \sim 58^\circ$. The 1D CP chain formed because of the extended coordination involving 3U further self-assembled with another neighboring chain sustained by N–H \cdots O hydrogen bonding involving the urea N–H and carboxylate O atoms of the interacting chains, resulting in hydrogen-bonded dimers that

were packed in a parallel fashion stabilized by dispersion forces (Figure 5).

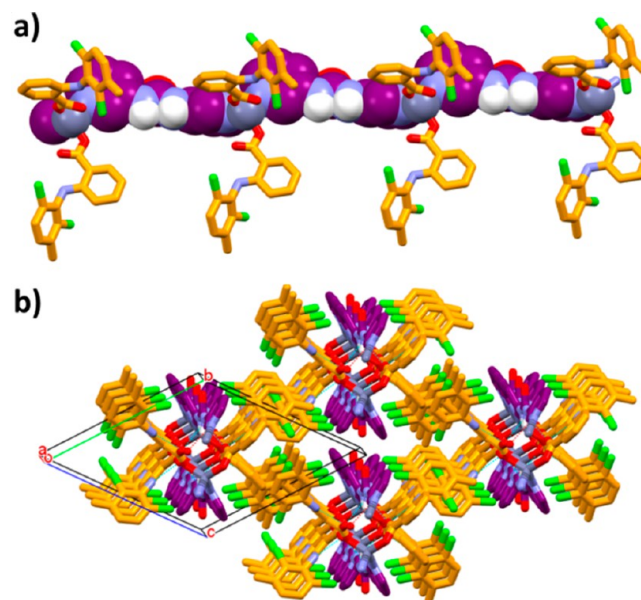


Figure 5. Crystal structure illustration of 3UMEC: (a) 1D CP chains with the anchored drug molecule MEC and (b) packing of the hydrogen-bonded dimer of the 1D CP chains viewed down the *a* axis.

Crystal Structure of 3UMEF. This compound crystallized in the centrosymmetric triclinic $P\bar{1}$ space group. The asymmetric unit contained one Zn(II) atom, one 3U ligand, and two MEF molecules, all located on general positions. The bidentate ligand 3U was involved in extended coordination with the Zn(II) metal ions, resulting in 1D CP chains on which the drug molecules were found to be anchored via unidentate coordination Zn(II) through carboxylate O atoms. The conformation of the ligand 3U was significantly nonplanar with $\Phi = \sim 65^\circ$, and the metal center displayed a distorted tetrahedral coordination geometry. The 1D CP chains were further self-assembled to form hydrogen-bonded dimers through N–H \cdots O interactions involving urea N–H and carboxylate O atoms of the interacting chains; such dimer chains were further packed in a parallel fashion sustained by dispersion forces (Figure 6).

Crystal Structure of 4UIBU. The crystal structure of 4UIBU was solved in the centrosymmetric monoclinic space group $P2_1/c$. One Zn(II) ion, one 4U ligand, two IBU ligands, and a lattice-occluded water molecule were located in the asymmetric unit. Both the methyl and one of the isopropyl groups of one of the IBU moieties were disordered over two positions (see the Experimental Section). The characteristic dihedral angle Φ of 4U was $\sim 24^\circ$, indicating a nonplanar conformation, and the Zn(II) ion showed distorted tetrahedral coordination geometry, wherein two sites were occupied by the pyridyl N atoms of two 4U ligands and the other two positions were coordinated by unidentate coordination of the carboxylate O atom of two IBU ligands. As a result, a 1D CP chain was formed on which the drug molecules were coordinated to the metal center. The 1D chains formed hydrogen-bonding interactions involving one of the urea N–H and carboxylate O atoms of the neighboring chain, and the interstitial space of the crystal lattice was occupied by the solvate water molecules

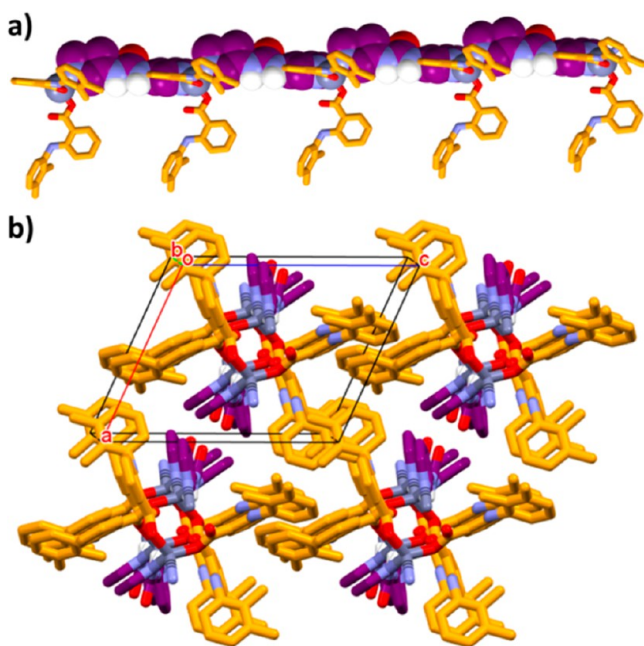


Figure 6. Crystal structure illustration of 3UMEF: (a) 1D CP chains with the anchored drug molecule MEF and (b) packing of the hydrogen-bonded dimer of the 1D CP chains viewed down the *b* axis.

sustained by N–H···O and O–H···O interactions involving the urea N–H and carboxylate O atoms (Figure 7).

Crystal Structure of 4UNAP. The crystal structure belonged to the noncentric monoclinic space group $P2_1$. The asymmetric unit contained two crystallographically independent moieties, each having one Zn(II) atom, one 4U ligand, and two NAP ligands. The NAP carboxylates displayed unidentate coordination to the metal center in both moieties. The urea ligand

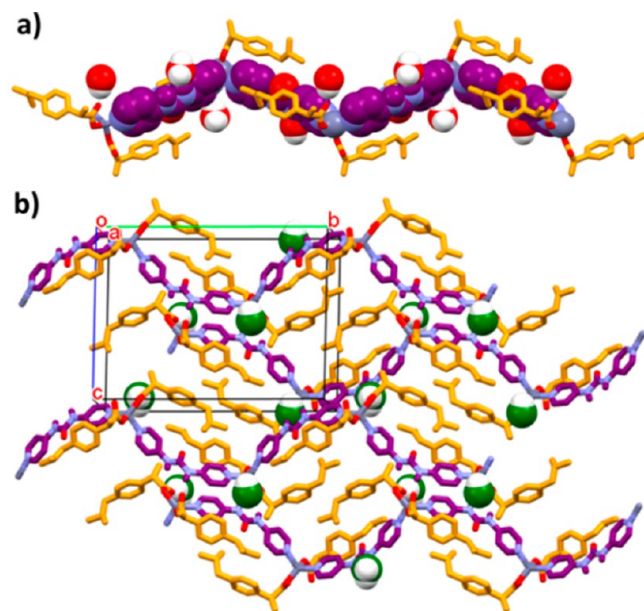


Figure 7. Crystal structure illustration of 4UIBU: (a) 1D CP chains with the anchored drug molecule IBU and hydrogen-bonded water molecules (in the space-filling model) and (b) overall packing of the hydrogen-bonded 1D CP chains with lattice-occluded water molecules (shown in the green space-filling model) viewed down the *a* axis.

showed a reasonably planar conformation ($\Phi = \sim 6$ and $\sim 5^\circ$), and the metal center displayed distorted tetrahedral geometry in both moieties. Because of the extended coordination of the pyridylurea ligand, each crystallographically independent moiety formed a 1D CP chain that interacted with another symmetry-equivalent 1D chain by N–H···O hydrogen bonding involving the urea N–H and carboxylate O atoms to form a dimer assembly; such an assembly of chains further packed in a parallel fashion sustained by dispersion forces (Figure 8).

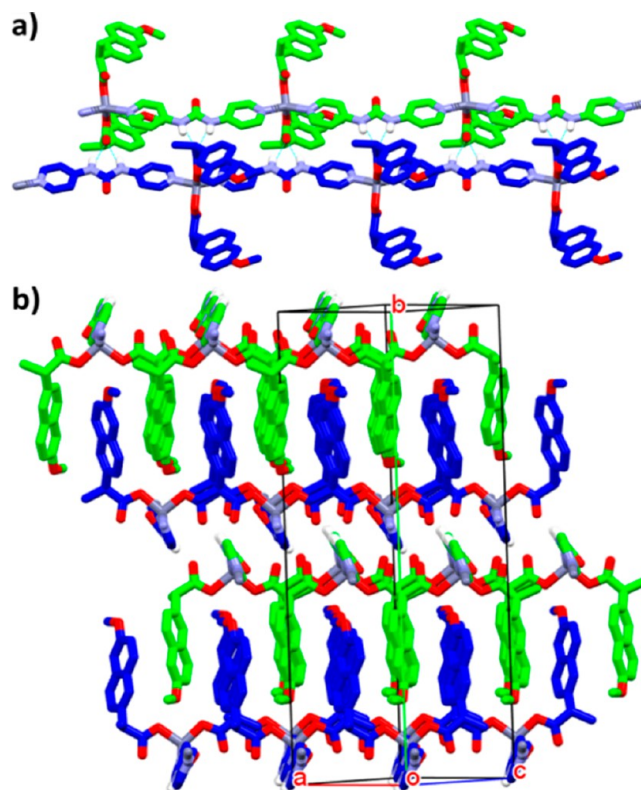


Figure 8. Crystal structure illustration of 4UNAP: (a) two crystallographically independent 1D CP chains (shown in different colors) with the anchored drug molecule NAP and (b) packing of the hydrogen-bonded dimer of the 1D CP chains viewed down the *ac* plane.

Crystal Structure of 4UFEN. The SXRD-refined model showed that 4UFEN crystallized in the centrosymmetric monoclinic space group $P2_1/n$. The asymmetric unit contained one Zn(II) ion, one 4U ligand, two IBU ligands, and one lattice-occluded water molecule. The bis(pyridyl)urea ligand 4U ($\Phi = \sim 25^\circ$) displayed an extended coordination mode with the Zn(II) metal centers, resulting in a 1D CP chain wherein the drug molecules remained anchored to the chain via unidentate coordination involving the carboxylates to Zn(II) metal centers. The polymer chains formed a hydrogen-bonded dimer involving one of the N–H bonds of the urea moiety and the carboxylate O atom of the interacting chains; the solvate water molecule occupied the interstitial space sustained by N–H···O and O–H···O hydrogen bonding involving the urea N–H and carboxylate O atom. Such a dimer assembly of the polymer chain further packed in a parallel fashion stabilized by dispersion forces (Figure 9).

The crystalline phase purity of the bulk samples of the CPs was found to be excellent to reasonably good, as revealed by

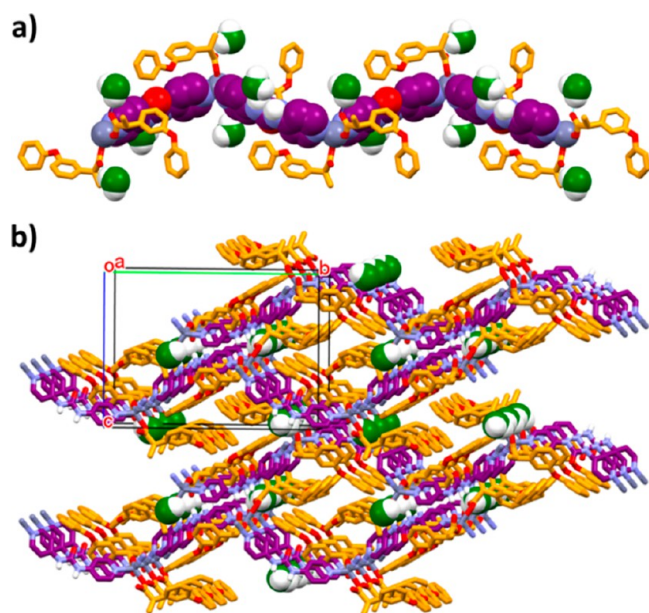


Figure 9. Crystal structure illustration of 4UFEN: (a) 1D CP chains with the anchored drug molecule FEN and hydrogen-bonded water molecules (in the space-filling model) and (b) overall packing of the hydrogen-bonded 1D CP chains with lattice-occluded water molecules (shown in the green space-filling model) viewed down the *a* axis.

comparing the PXRD patterns of the bulk sample and the corresponding simulated PXRD patterns obtained from the SXRD data (Figures S27–S35) except for 3UIBU; the major mismatch of the PXRD patterns in this case might be due to the formation of a polymorph during crystallization of the CP. The foregoing discussions on the crystal structures of the isolated OIHSs clearly highlighted a few key features that were expected to be useful for developing metallogel-based DDSs: (a) drug molecules were part of the OIHSs, thereby getting rid of the difficulties involved in drug loading; (b) all of the crystal structures were 1D CPs having hydrogen-bonding-capable moieties [the urea functionality of the bis(pyridyl)urea ligands 3U and 4U and carboxylate O atoms of the drug molecules] that helped self-assemble the 1D chains and, in three cases (3UNAP, 4UIBU, and 4UFEN), interacted strongly with lattice-occluded solvates (water), key features for gelation (vide supra). Besides, the conformational flexibility of the bis(pyridyl)urea ligands, as revealed from the wide range of dihedral angles $\Phi = 6\text{--}65^\circ$ of the terminal pyridyl rings (Scheme 1), was expected to contribute toward effective interactions in the presence of polar solvents facilitating gelation.

Metallogelation. SXRD analyses revealed that, in all CPs, the ratio of the reactants, i.e., metal/ligand/NSAID, was 1:1:2. We, therefore, decided to carry out metallogelation studies with this reactant ratio for all nine CPs. Interestingly, as many as five metallogels (3UNAPg, 3UMECg, 3UMEFg, 4UNAPg, and 4UFENg) were obtained and the reaction of $\text{Zn}(\text{NO}_3)_2$, 4U, and MEF under identical conditions also produced metallogel 4UMEFg. It may be noted that, under identical conditions, 3U produced a gelatinous precipitate and colloidal solutions when treated with IBU, DIC, and FEN, respectively, whereas 4U generated a precipitate, a gelatinous precipitate, and a colloidal solution when treated with IBU, MEC, and DIC, respectively. In a typical experiment, when an aqueous

solution of $\text{Zn}(\text{NO}_3)_2$ was added to a DMSO solution containing the urea ligand and NSAID, instantaneous gelation occurred at room temperature, as confirmed by an “inverted vial” test wherein the gel was able to sustain its own weight against gravity (Scheme 2 and Table S11). All of the gels were thermoirreversible, indicating the CP nature of the gelator, stable for a few days, and precipitated out with aging. To confirm that they were really gels, we carried out dynamic rheology of the gels. Gel, being a non-Newtonian liquid, shows a viscoelastic response in dynamic rheology; a plot of G' (storage modulus) and G'' (viscous modulus) versus angular velocity ω (rad/s) under a constant strain chosen from the LVE region obtained from amplitude sweep experiments would show that G' is much larger than G'' and largely frequency-invariant at low ω , i.e., longer time scale.⁵⁶ The nice viscoelastic response in all cases indicated that all of these materials that passed through all “inverted vial” tests were indeed gels (Figure 10). The gels had reasonable mechanical strength, with $\tan \delta$ ranging from 0.09 to 0.15 (Table S11).

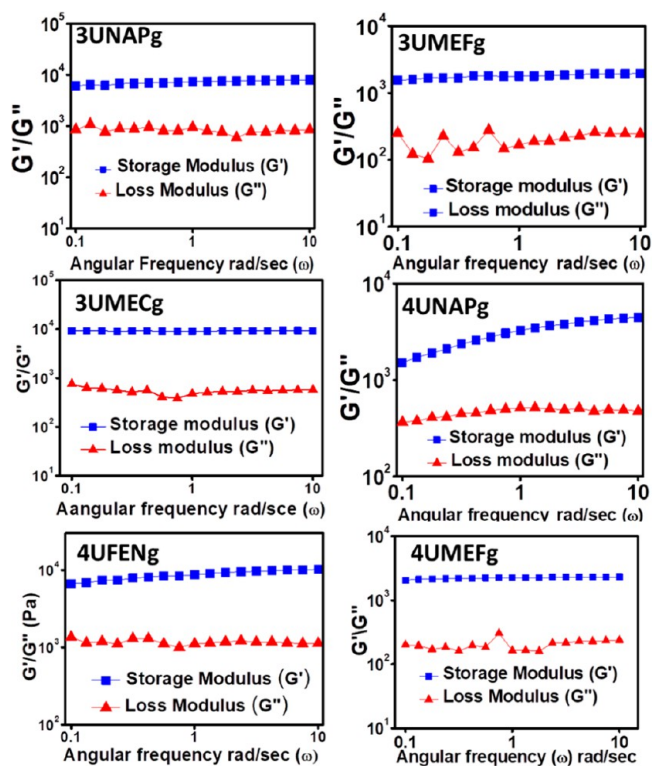


Figure 10. Viscoelastic (gel-like) response of the metallogels in dynamic rheology.

It is interesting to note that, in all five cases for which we have single-crystal structures, the PXRD patterns of the dried gel (xerogel) showed significant correspondence with that obtained from the bulk sample, with the SXRD data (simulated) indicating that the gel network essentially represented that observed in the single-crystal structures (Figures S37–S41). However, one cannot rule out the possibility of having different crystalline phases of the xerogel in minor amounts because of the fact that a complete match of the PXRD patterns was not observed; evaporation of the solvent during xerogel formation might be the driving force for the formation of different crystalline phases in minor amounts.

Thus, the rationale employed herein to design metallogelators seemed to have worked to a significant extent.

The morphology of the gel networks was studied by TEM. Figure 11 displayed networks of entangled fibers for 3UNAPg,

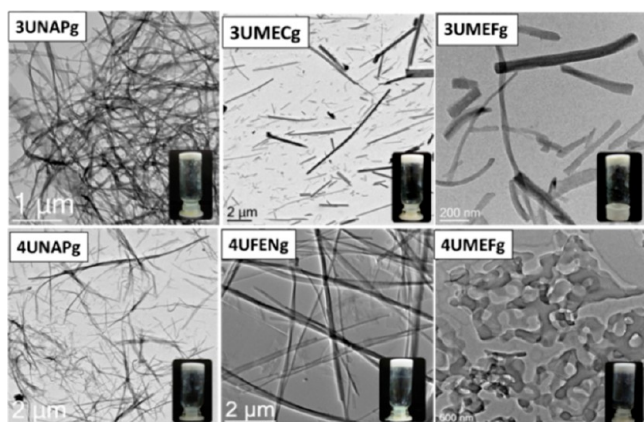


Figure 11. Metallogel network morphology under TEM. Insets: Inverted vial pictures of the corresponding gels.

4UNAPg, 4UFENG, and 4UMEFg typically observed for gels. However, 3UMECg and 3UMEFg showed discrete short fibers, which were also not so uncommon for gels.^{57–59}

Biological Studies. Anticancer Property of the Metallogelators. Because the NSAIDs were now part of the coordination network and many of them did possess anticancer properties,^{60,61} we explored the effect of metallogelators on cancer cells. For this purpose, we carried out MTT assay⁶² on the murine tumor melanoma cell line (B16F10) in the presence of crystallographically characterized metallogelators. The B16F10 cell line was chosen because it is used as a model for human skin cancer, and therefore the corresponding metallogel could be applied topically. MTT assay revealed that 3UMEF possessed the best ability to kill the cancer cells with $IC_{50} = 80 \mu\text{g/mL}$ (Figure S42). We, therefore, decided to carry out further experiments with 3UMEF. Cell migration assay or

scratch assay was employed to evaluate the anticancer property of the metallogelator 3UMEF. While the orchestrated migration of cells in a particular direction is important for any multicellular organism for its development and maintenance, cancer cells display uncontrolled migration, leading to invasion and metastasis.⁶³ Thus, the ability to inhibit cancer cell migration by a potential anticancer agent is estimated by determining the speed with which the cancer cells migrate under in vitro conditions in the presence of the agent; the slower the speed, the better the anticancer property of the agent.⁶⁴ Scratch assay was performed on B16F10 cells using only media (control), the ligand 3U, the NSAID component, i.e., mefenamic acid (MEFH), and the metallogelator 3UMEF. The cell migration speed was lowest ($4.9 \mu\text{M/h}$) for 3UMEF, establishing the beneficiary effect of the metallogelator as an anticancer agent compared to that of its individual components (Figure 12). These data clearly suggested that the metallogelator 3UMEF must have been internalized by the cancer cells.

Cell Imaging. In order to probe the cell permeability of the metallogelators, we selected 3UNAP for cell imaging studies because the naproxen moiety of 3UNAP does have moderate green emission in fluorescence when excited in the blue region. LSM of B16F10 cells in the presence of 3UNAP and a nucleus staining dye DAPI clearly confirmed that 3UNAP was successfully internalized, as is evident from the green and blue fluorescence due to 3UNAP and DAPI in the cytosol and nucleus, respectively (Figure 13).

Conventional Drug Delivery: Exploring Antibacterial and Multidrug-Delivery Applications. To explore the possibility of using one of the metallogels for antibacterial and multidrug-delivery applications following conventional a drug-delivery route, we chose to work with 3UMECg because of its stability and bright-white color. We allowed a AgNO_3 solution to soak into the 3UMECg gel bed and exposed it to laboratory light for 24 h. The appearance of a dark-violet color in the gel bed indicated the formation of AgNPs.⁸¹ The TEM image of $\text{AgNP}@3\text{UMECg}$ revealed that the nanoparticles were adhered to the gel network and the sizes of the AgNPs were

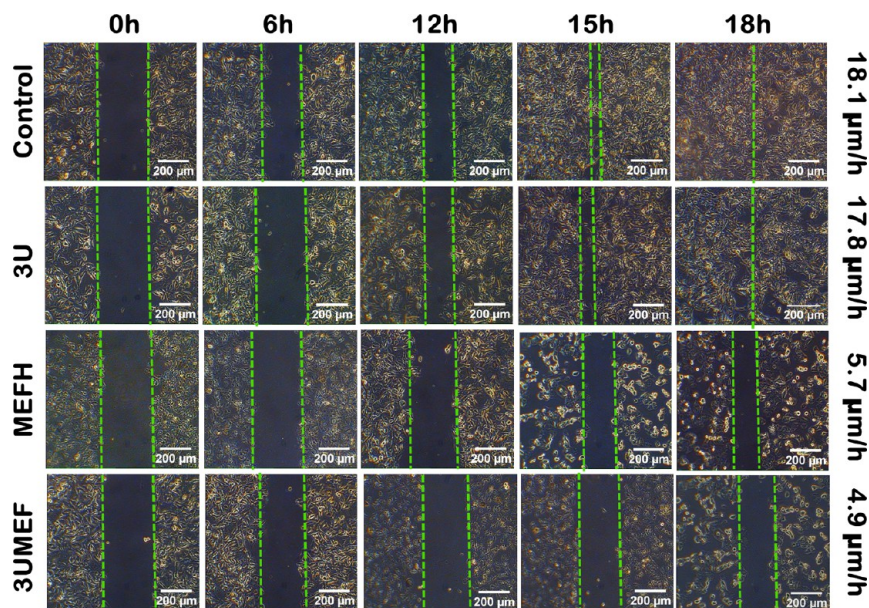


Figure 12. Scratch assay: B16F10 cell migration under various conditions.

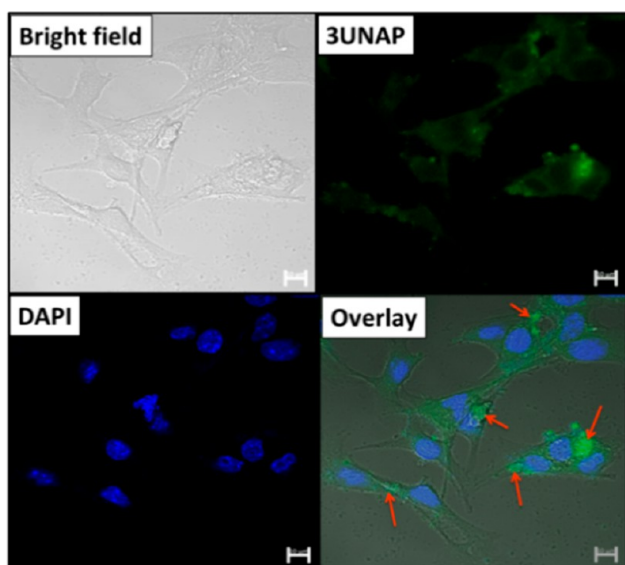


Figure 13. LSCM images of B16F10 cells under various conditions (scale bar = 20 μm).

~ 15 nm. Selected-area electron diffraction of the TEM image showed nice diffraction spots, indicating the crystalline nature of the AgNPs. Energy-dispersive X-ray spectroscopy also revealed the presence of Ag in the TEM image. The UV-vis spectrum of the AgNPs in DMSO also showed a characteristic surface plasmon peak at ~ 458 nm. These data clearly demonstrated that AgNPs indeed formed within 3UMECg; it may be mentioned that the formation of metal nanoparticles without the assistance of an external reducing agent might have been facilitated by the urea moiety of 3U in the metallogel because urea as well as amide moieties are known to act as reducing agents for such a purpose.^{65,66} Sometimes solvents such as *N,N*-dimethylformamide could also act as reducing agents in synthesizing AgNPs.⁸² Interestingly, the PXRD pattern of AgNP@3UMECg matched quite well with that of simulated, bulk, and xerogel of 3UMECg, suggesting that the formation of AgNPs within the metallogel did not alter the

network structure of the xerogel of 3UMECg (Figure 14a). The antibacterial property of AgNPs is well documented.^{67–69} Therefore, AgNP@3UMECg can be used for antibacterial application (vide infra).

To load another drug into the gel matrix for plausible multidrug-delivery application, we soaked the 3UMECg gel bed with a solution containing a NSAID, namely, sulfasalazine (SUL). The bright-yellow color of SUL helped us to visualize its intake by the gel bed. The loading efficiency of the drug within the gel matrix was found to be $\sim 51\%$ (Figures S43 and S44). Steady release of the drug from the SUL@3UMECg gel bed to PBS was also monitored by UV-vis; a gradual increase in the intensity of $\lambda = \sim 366$ nm with time indicated the release of SUL into the bulk solvent. The percentage of release of SUL from SUL@3UMECg was $\sim 73\%$ (Figures 14b and S45). The morphology of the gel network of SUL@3UMECg observed under TEM was similar to that found for 3UMECg, indicating that adsorption of the drug did not have any effect on the supramolecular architecture of the metallogel. It was interesting to note that both of the metallogels 3UMECg and SUL@3UMECg could be spread on a Petri dish and the characteristic color of SUL in SUL@3UMECg (yellow and green) was visible under visible and UV light, respectively (Figure 14b).

We demonstrated that the cargos in both AgNP@3UMECg and SUL@3UMECg could be delivered in vitro. For this purpose, we cut four grooves in an agar plate inoculated with a Gram-negative bacterium, namely, *Klebsiella* spp. The grooves were filled with nothing (control), 3UMECg, SUL@3UMECg, and AgNP@3UMECg and incubated at 37 $^{\circ}\text{C}$ for 24 h. Evidence of an inhibited zone (15 ± 2 mm) around the groove containing AgNP@3UMECg confirmed the delivery of antibacterial AgNPs, whereas no such inhibited zones around the grooves containing nothing and 3UMECg were observed. The bright-yellow color due to the diffusion of SUL into agar gel around the groove containing SUL@3UMECg suggested its successful delivery under in vitro conditions. Finally, the shear-thinning property of 3UMECg required for topical application was demonstrated by rheoreversibility as well as by

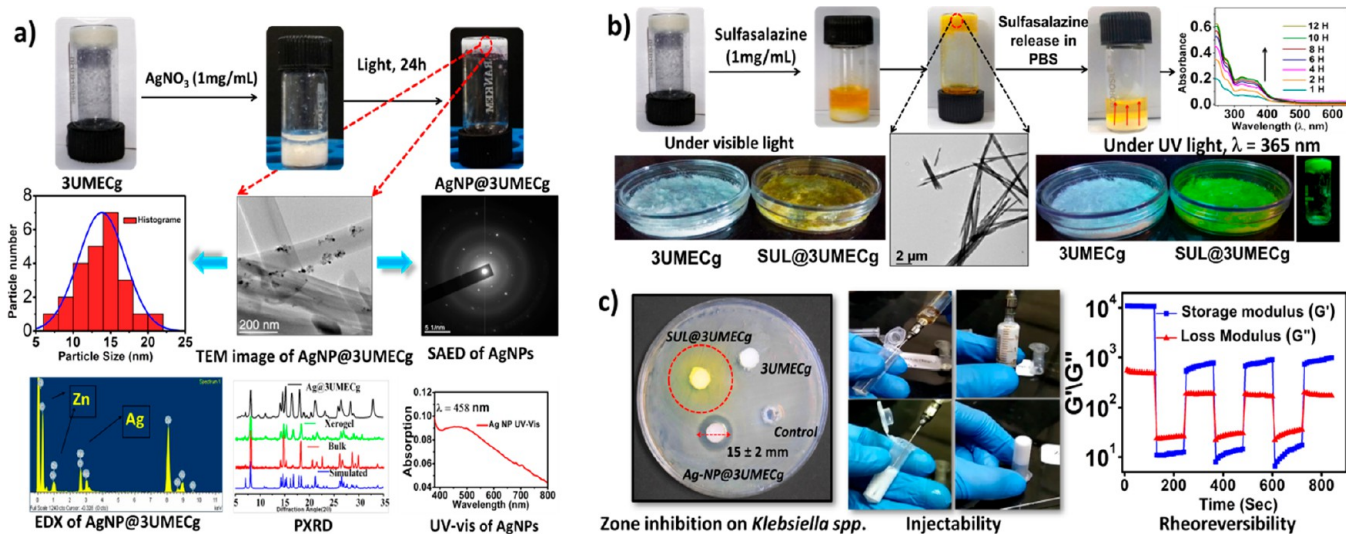


Figure 14. (a) Synthesis and characterization AgNPs inside 3UMECg. (b) Loading and release of the drug SUL using the 3UMECg gel matrix. (c) Zone inhibition and shear thinning of 3UMECg.

drawing of the gel into a syringe and then syringing it out into a vial without phase separation (Figure 14c and video).

CONCLUSION

Thus, we have successfully demonstrated that structural rationale could indeed be employed to synthesize a new series of OIHSs that not only incorporated the drug molecules (NSAIDs) in the coordination network, thereby getting rid of the need for loading of the drug into a vehicle, but also provided a series of metallogels. While the metallogelator 3UMEF showed anticancer behavior against the B16F10 cell line (MTT and cell migration assay), 3UNAP was successfully internalized by the cancer cells (LSCM with DAPI), thereby suggesting the possibility of exploring the metallogel 3UMEFg as a topical gel for self-drug-delivery application for the treatment of skin cancer. The successful synthesis of AgNPs within the metallogel 3UMECg and its in vitro delivery to inhibit the growth of Gram-negative bacterium *Klebsiella* spp. and the loading and delivery of another NSAID, namely, SUL, using 3UMECg as a gel matrix suggested utility of the metallogels for the development of conventional DDSs with a potential for multidrug delivery. Although DMSO is known to facilitate skin penetration of drugs including NSAIDs in topical application,⁸³ the amount of DMSO required to form the metallogels studied herein may have an adverse toxic effect. Therefore, the present data mainly support the proof of concept and should be considered as a model for in vitro drug release. Research toward the development of such metallogels from pure water or aqueous solvent systems containing safe amounts of DMSO is required for real-life application.

ASSOCIATED CONTENT

Supporting Information

The Supporting Information is available free of charge at <https://pubs.acs.org/doi/10.1021/acs.inorgchem.0c03550>.

Synthesis and characterization of the ligands, FT-IR, ORTEP, hydrogen bond table of the CPs, PXRD patterns, rheological data, MTT assay, and sulfasalazine absorption and release (PDF)

Z-stack animation (AVI)

Instantaneous gelation and injectable metallogel (MP4)

Accession Codes

CCDC 1878233–1878241 contain the supplementary crystallographic data for this paper. These data can be obtained free of charge via www.ccdc.cam.ac.uk/data_request/cif, or by emailing data_request@ccdc.cam.ac.uk, or by contacting The Cambridge Crystallographic Data Centre, 12 Union Road, Cambridge CB2 1EZ, UK; fax: +44 1223 336033.

AUTHOR INFORMATION

Corresponding Author

Parthasarathi Dastidar – School of Chemical Sciences, Indian Association for the Cultivation of Science, Kolkata 700032, India; orcid.org/0000-0002-1011-2386; Email: ocpd@iacs.res.in

Author

Protap Biswas – School of Chemical Sciences, Indian Association for the Cultivation of Science, Kolkata 700032, India

Complete contact information is available at: <https://pubs.acs.org/doi/10.1021/acs.inorgchem.0c03550>

Author Contributions

All authors have given approval to the final version of the manuscript.

Notes

The authors declare no competing financial interest.

ACKNOWLEDGMENTS

P.D. thanks DST (CRG/2019/000790) for financial support. A SXR facility was availed at the Department of Organic Chemistry, IACS, supported by the CEIB program of DBT (BT/01/CEIB/11/V/13). P.B. acknowledges IACS for a fellowship. P.B. thanks Dr. Hemanta K. Datta for help pertaining to the antibacterial experiments.

REFERENCES

- (1) Yaghi, O. Reticular Chemistry-Construction, Properties, and Precision Reactions of Frameworks. *J. Am. Chem. Soc.* **2016**, *138*, 15507–15509 and references cited therein.
- (2) Fernández-Paz, C.; Rojas, S.; Salcedo-Abraira, P.; Simón-Yarza, T.; Remuñán-López, C.; Horcajada, P. Metal-Organic Framework Microsphere Formulation for Pulmonary Administration. *ACS Appl. Mater. Interfaces* **2020**, *12*, 25676–25682.
- (3) Velásquez-Hernández, M. D. J.; Astria, E.; Winkler, S.; Liang, W.; Wiltsche, H.; Poddar, A.; Shukla, R.; Prestwich, G.; Paderi, J.; Salcedo-Abraira, P.; Amenitsch, H.; Horcajada, P.; Doonan, C. J.; Falcaro, P. Modulation of metal-azolate frameworks for the tunable release of encapsulated glycosaminoglycans. *Chemical Science* **2020**, *11*, 10835–10843.
- (4) Abánades Lázaro, I.; Forgan, R. S. Application of zirconium MOFs in drug delivery and biomedicine. *Coord. Chem. Rev.* **2019**, *380*, 230–259.
- (5) Carrillo-Carrión, C.; Martínez, R.; Navarro Poupard, M. F.; Pelaz, B.; Polo, E.; Arenas-Vivo, A.; Olgiati, A.; Taboada, P.; Soliman, M. G.; Catalán, Ú.; Fernández-Castillejo, S.; Solà, R.; Parak, W. J.; Horcajada, P.; Alvarez-Puebla, R. A.; del Pino, P. Aqueous Stable Gold Nanostar/ZIF-8 Nanocomposites for Light-Triggered Release of Active Cargo Inside Living Cells. *Angew. Chem., Int. Ed.* **2019**, *58*, 7078–7082.
- (6) Taylor-Pashow, K. M. L.; Della Rocca, J.; Xie, Z.; Tran, S.; Lin, W. Postsynthetic Modifications of Iron-Carboxylate Nanoscale Metal-Organic Frameworks for Imaging and Drug Delivery. *J. Am. Chem. Soc.* **2009**, *131*, 14261–14263.
- (7) Kundu, T.; Mitra, S.; Patra, P.; Goswami, A.; Díaz Díaz, D.; Banerjee, R. Mechanical Downsizing of a Gadolinium(III)-based Metal-Organic Framework for Anticancer Drug Delivery. *Chem. - Eur. J.* **2014**, *20*, 10514–10518.
- (8) Ibrahim, M.; Sabouni, R.; Hussein, G. A. Anti-cancer drug delivery using metal organic frameworks (MOFs). *Curr. Med. Chem.* **2017**, *24*, 193–214.
- (9) Levine, D. J.; Runčevski, T.; Kapelewski, M. T.; Keitz, B. K.; Oktawiec, J.; Reed, D. A.; Mason, J. A.; Jiang, H. Z. H.; Colwell, K. A.; Legendre, C. M.; Fitz-Gerald, S. A.; Long, J. R. Olsalazine-Based Metal-Organic Frameworks as Biocompatible Platforms for H₂ Adsorption and Drug Delivery. *J. Am. Chem. Soc.* **2016**, *138*, 10143–10150.
- (10) Wu, M.-X.; Yang, Y.-W. Metal-Organic Framework (MOF)-Based Drug/Cargo Delivery and Cancer Therapy. *Adv. Mater.* **2017**, *29*, 1606134.
- (11) Soppimath, K. S.; Aminabhavi, T. M.; Kulkarni, A. R.; Rudzinski, W. E. Biodegradable polymeric nanoparticles as drug delivery devices. *J. Controlled Release* **2001**, *70*, 1–20.
- (12) Cao, Z.; Tong, R.; Mishra, A.; Xu, W.; Wong, G. C. L.; Cheng, J.; Lu, Y. Reversible Cell-Specific Drug Delivery with Aptamer-Functionalized Liposomes. *Angew. Chem., Int. Ed.* **2009**, *48*, 6494–6498.

- (13) Urich, K. E.; Cannizzaro, S. M.; Langer, R. S.; Shakesheff, K. M. Polymeric Systems for Controlled Drug Release. *Chem. Rev.* **1999**, *99*, 3181–3198.
- (14) Mintzer, M. A.; Grinstaff, M. W. Biomedical applications of dendrimers: a tutorial. *Chem. Soc. Rev.* **2011**, *40*, 173–190.
- (15) Caminade, A. M.; Turrin, C. O. Dendrimers for drug delivery. *J. Mater. Chem. B* **2014**, *2*, 4055–4066.
- (16) Michalet, X.; Pinaud, F. F.; Bentolila, L. A.; Tsay, J. M.; Doose, S.; Li, J. J.; Sundaresan, G.; Wu, A. M.; Gambhir, S. S.; Weiss, S. Quantum Dots for Live Cells, in Vivo Imaging, and Diagnostics. *Science* **2005**, *307*, 538–544.
- (17) Rosi, N. L.; Mirkin, C. A. Nanostructures in Biodiagnostics. *Chem. Rev.* **2005**, *105*, 1547–1562.
- (18) Kim, J.; Kim, H. S.; Lee, N.; Kim, T.; Kim, H.; Yu, T.; Song, I. C.; Moon, W. K.; Hyeon, T. Multifunctional Uniform Nanoparticles Composed of a Magnetite Nanocrystal Core and a Mesoporous Silica Shell for Magnetic Resonance and Fluorescence Imaging and for Drug Delivery. *Angew. Chem., Int. Ed.* **2008**, *47*, 8438–8441.
- (19) Doane, T. L.; Burda, C. The unique role of nanoparticles in nanomedicine: imaging, drug delivery and therapy. *Chem. Soc. Rev.* **2012**, *41*, 2885–2911.
- (20) Dreaden, E. C.; Mackey, M. A.; Huang, X.; Kang, B.; El-Sayed, M. A. Beating cancer in multiple ways using nanogold. *Chem. Soc. Rev.* **2011**, *40*, 3391–3404.
- (21) Horcajada, P.; Serre, C.; Vallet-Regí, M.; Sebban, M.; Taulelle, F.; Férey, G. Metal-Organic Frameworks as Efficient Materials for Drug Delivery. *Angew. Chem., Int. Ed.* **2006**, *45*, 5974–5978.
- (22) Bellido, E.; Hidalgo, T.; Lozano, M. V.; GuilleVIC, M.; Simón-Vázquez, R.; Santander-Ortega, M. J.; González-Fernández, A.; Serre, C.; Alonso, M. J.; Horcajada, P. Heparin-Engineered Mesoporous Iron Metal-Organic Framework Nanoparticles: Toward Stealth Drug Nanocarriers. *Adv. Healthcare Mater.* **2015**, *4*, 1246–1257.
- (23) Cunha, D.; Ben Yahia, M.; Hall, S.; Miller, S. R.; Chevreau, H.; Elkaim, E.; Maurin, G.; Horcajada, P.; Serre, C. Rationale of Drug Encapsulation and Release from Biocompatible Porous Metal-Organic Frameworks. *Chem. Mater.* **2013**, *25*, 2767–2776.
- (24) Chen, W.-H.; Yu, X.; Liao, W.-C.; Sohn, Y. S.; Ceconello, A.; Kozell, A.; Nechushtai, R.; Willner, I. ATP-Responsive Aptamer-Based Metal-Organic Framework Nanoparticles (NMOFs) for the Controlled Release of Loads and Drugs. *Adv. Funct. Mater.* **2017**, *27*, 1702102.
- (25) Wang, Y.; Yan, J.; Wen, N.; Xiong, H.; Cai, S.; He, Q.; Hu, Y.; Peng, D.; Liu, Z.; Liu, Y. Metal-organic frameworks for stimuli-responsive drug delivery. *Biomaterials* **2020**, *230*, 119619.
- (26) Pander, M.; Żelichowska, A.; Bury, W. Probing mesoporous Zr-MOF as drug delivery system for carboxylate functionalized molecules. *Polyhedron* **2018**, *156*, 131–137.
- (27) Ma, Z.; Moulton, B. Supramolecular Medicinal Chemistry: Mixed-Ligand Coordination Complexes. *Mol. Pharmaceutics* **2007**, *4*, 373–385.
- (28) Ma, Z.; Moulton, B. Mixed-Ligand Coordination Species: A Promising Approach for “Second-Generation” Drug Development. *Cryst. Growth Des.* **2007**, *7*, 196–198.
- (29) Yang, Z.; Liang, G.; Xu, B. Enzymatic Hydrogelation of Small Molecules. *Acc. Chem. Res.* **2008**, *41*, 315–326.
- (30) Zhao, F.; Ma, M. L.; Xu, B. Molecular hydrogels of therapeutic agents. *Chem. Soc. Rev.* **2009**, *38*, 883–891.
- (31) Foster, J. A.; Steed, J. W. Exploiting Cavities in Supramolecular Gels. *Angew. Chem., Int. Ed.* **2010**, *49*, 6718–6724.
- (32) Terech, P.; Weiss, R. G. Low Molecular Mass Gelators of Organic Liquids and the Properties of Their Gels. *Chem. Rev.* **1997**, *97*, 3133–3159.
- (33) Tomasini, C.; Castellucci, N. Peptides and peptidomimetics that behave as low molecular weight gelators. *Chem. Soc. Rev.* **2013**, *42*, 156–172.
- (34) Weiss, R. G.; Terech, P., Eds. *Molecular Gels: Materials with Self-Assembled Fibrillar Networks*; Springer: Dordrecht, The Netherlands, 2006.
- (35) Hirst, A. R.; Escuder, B.; Miravet, J. F.; Smith, D. K. High-Tech Applications of Self-Assembling Supra-molecular Nanostructured Gel-Phase Materials: From Regenerative Medicine to Electronic Devices. *Angew. Chem., Int. Ed.* **2008**, *47*, 8002–8018.
- (36) Suzuki, M.; Hanabusa, K. L-Lysine-based low-molecular-weight gelators. *Chem. Soc. Rev.* **2009**, *38*, 967–975.
- (37) Piepenbrock, M.-O. M.; Lloyd, G. O.; Clarke, N.; Steed, J. W. Metal- and Anion-Binding Supramolecular Gels. *Chem. Rev.* **2010**, *110*, 1960–2004.
- (38) Du, X.; Zhou, J.; Shi, J.; Xu, B. Supramolecular Hydrogelators and Hydrogels: From Soft Matter to Molecular Biomaterials. *Chem. Rev.* **2015**, *115*, 13165–13307.
- (39) Zelzer, M.; Todd, S. J.; Hirst, A. R.; McDonald, T. O.; Ulijn, R. V. Enzyme responsive materials: design strategies and future developments. *Biomater. Sci.* **2013**, *1*, 11–39.
- (40) Singh, N.; Conte, M. P.; Ulijn, R. V.; Miravet, J. F.; Escuder, B. Insight into the esterase like activity demonstrated by an imidazole appended self-assembling hydrogelator. *Chem. Commun.* **2015**, *51*, 13213–13216.
- (41) Lalitha, K.; Prasad, Y. S.; Maheswari, C. U.; Sridharan, V.; John, G.; Nagarajan, S. Stimuli responsive hydrogels derived from a renewable resource: synthesis, self-assembly in water and application in drug delivery. *J. Mater. Chem. B* **2015**, *3*, 5560–5568.
- (42) Vemula, P. K.; Wiradharma, N.; Ankrum, J. A.; Miranda, O. R.; John, G.; Karp, J. M. Prodrugs as self-assembled hydrogels: a new paradigm for biomaterials. *Curr. Opin. Biotechnol.* **2013**, *24*, 1174–1182.
- (43) Dastidar, P.; Roy, R.; Parveen, R.; Sarkar, K. Supramolecular Synthon Approach in Designing Molecular Gels for Advanced Therapeutics. *Adv. Therap.* **2019**, *2*, 1800061.
- (44) Dastidar, P. Designing Supramolecular Gelators: Challenges, Frustrations, and Hopes. *Gels* **2019**, *5*, 15 and references cited therein.
- (45) Sarkar, K.; Khasimbi, S.; Mandal, S.; Dastidar, P. Rationally Developed Metallogelators Derived from Pyridyl Derivatives of NSAIDs Displaying Anti-Inflammatory and Anticancer Activities. *ACS Appl. Mater. Interfaces* **2018**, *10*, 30649–30661.
- (46) Roy, R.; Bhagyalalitha, M.; Choudhury, P.; Dastidar, P. Salt metathesis for developing injectable supramolecular metallohydrogelators as a multi-drug-self-delivery system. *Chem. Commun.* **2016**, *52*, 13811–13814.
- (47) Sheldrick, G. A short history of SHELX. *Acta Crystallogr., Sect. A: Found. Crystallogr.* **2008**, *64*, 112–122.
- (48) Dolomanov, O. V.; Bourhis, L. J.; Gildea, R. J.; Howard, J. A. K.; Puschmann, H. OLEX2: A complete structure solution, refinement and analysis program. *J. Appl. Crystallogr.* **2009**, *42*, 339–341.
- (49) Dastidar, P. Supramolecular gelling agents: can they be designed? *Chem. Soc. Rev.* **2008**, *37*, 2699–2715.
- (50) James, S. L.; Lloyd, G. O.; Zhang, J. Supramolecular gels in crystal engineering. *CrystEngComm* **2015**, *17*, 7976–7977.
- (51) van Esch, J. H.; Feringa, B. L. New Functional Materials Based on Self-Assembling Organogels: From Serendipity towards Design. *Angew. Chem., Int. Ed.* **2000**, *39*, 2263–2266.
- (52) Dastidar, P.; Ganguly, S.; Sarkar, K. Metallogels from Coordination Complexes, Organometallic, and Coordination Polymers. *Chem. - Asian J.* **2016**, *11*, 2484–2498.
- (53) Xing, B.; Choi, M.-F.; Xu, B. A stable metal coordination polymer gel based on a calix [4] arene and its ‘uptake’ of non-ionic organic molecules from the aqueous phase. *Chem. Commun.* **2002**, 362–363.
- (54) Adarsh, N. N.; Sahoo, P.; Dastidar, P. Is a Crystal Engineering Approach Useful in Designing Metallogels? A Case Study. *Cryst. Growth Des.* **2010**, *10*, 4976–4986.
- (55) Lebel, O.; Perron, M.É.; Maris, T.; Zalzal, S. F.; Nanci, A.; Wuest, J. D. A New Class of Selective Low-Molecular-Weight Gelators Based on Salts of Diaminotriazinecarboxylic Acids. *Chem. Mater.* **2006**, *18*, 3616–3626.
- (56) Raghavan, S. R.; Douglas, J. F. The conundrum of gel formation by molecular nanofibers, wormlike micelles, and filamentous proteins: gelation without cross-links? *Soft Matter* **2012**, *8*, 8539–8546.

- (57) Chakraborty, P.; Das, B.; Pal, P.; Datta, S.; Bera, S.; Dastidar, P. A supramolecular hydrogel derived from a simple organic salt capable of proton conduction. *Chem. Commun.* **2020**, *56*, 5251–5254.
- (58) Sutar, P.; Suresh, V. M.; Jayaramulu, K.; Hazra, A.; Maji, T. K. Binder driven self-assembly of metal-organic cubes towards functional hydrogels. *Nat. Commun.* **2018**, *9*, 3587.
- (59) Ghosh, R.; Chakraborty, A.; Maiti, D. K.; Puranik, V. G. Crystal or Low Molecular Mass Organogel Based on Sugar-Derived Chiral Pyrano[2,3]naphtho[1,2]pyrans. *Org. Lett.* **2006**, *8* (6), 1061–1064.
- (60) Shacter, E.; Weitzman, S. A. Chronic inflammation and cancer. *Oncology* **2002**, *16*, 217–226.
- (61) Balkwill, F.; Mantovani, A. Inflammation and cancer: back to Virchow? *Lancet* **2001**, *357*, 539–545.
- (62) van Meerloo, J.; Kaspers, G. J.; Cloos, J. Cell sensitivity assays: the MTT assay. *Methods Mol. Biol.* **2011**, *731*, 237–245.
- (63) Deb, J.; Majumder, J.; Bhattacharyya, S.; Jana, S. S. A novel naproxen derivative capable of displaying anti-cancer and anti-migratory properties against human breast cancer cells. *BMC Cancer* **2014**, *14*, 567–574.
- (64) Cory, G. In *Scratch-wound assay: Methods in Molecular Biology Cell Migration Developmental Methods and Protocols*; Wells, C. M., Parsons, M., Eds.; Springer: London, 2011; pp 25–30.
- (65) Dutta, S.; Shome, A.; Debnath, S.; Das, P. K. Counterion dependent hydrogelation of amino acid based amphiphiles: switching from non-gelators to gelators and facile synthesis of silver nanoparticles. *Soft Matter* **2009**, *5*, 1607–1620.
- (66) Coates, A. L.; Smith, D. K. Hierarchical assembly—dynamic gel-nanoparticle hybrid soft materials based on biologically derived building blocks. *J. Mater. Chem.* **2010**, *20*, 6696–6702.
- (67) Rizzello, L.; Pompa, P. P. Nanosilver-based antibacterial drugs and devices: Mechanisms, methodological drawbacks, and guidelines. *Chem. Soc. Rev.* **2014**, *43*, 1501–1518.
- (68) Piras, C. C.; Mahon, C. S.; Smith, D. K. Self-Assembled Supramolecular Hybrid Hydrogel Beads Loaded with Silver Nanoparticles for Antimicrobial Applications. *Chem. - Eur. J.* **2020**, *26*, 8452–8457.
- (69) Song, J.; Yuan, C.; Jiao, T.; Xing, R.; Yang, M.; Adams, D. J.; Yan, X. H. Multifunctional Antimicrobial Biometallohydrogels Based on Amino Acid Coordinated Self-Assembly. *Small* **2020**, *16*, 1907309.
- (70) Zhang, Z.; Li, Y.; Geng, L.; Feng, G.; Ren, J.; Yu, X. Healable, Phase-Selective, and White-Light-Emitting Titania Based Hybrid Lanthanide-Doped Metallogels. *Inorg. Chem.* **2020**, *59*, 3974–3982.
- (71) Ma, Z.; Zhang, P.; Yu, X.; Lan, H.; Li, Y.; Xie, D.; Li, J.; Yi, T. Sugar based nanotube assembly for the construction of sonication triggered hydrogel: an application of the entrapment of tetracycline hydrochloride. *J. Mater. Chem. B* **2015**, *3*, 7366–7371.
- (72) Cao, L.; Wang, P.; Miao, X.; Duan, H.; Wang, H.; Dong, Y.; Ma, R.; Zhang, B.; Wu, B.; Li, X.; Stang, P. J. Diamondoid Frameworks via Supramolecular Coordination: Structural Characterization, Metallogel Formation, and Adsorption Study. *Inorg. Chem.* **2019**, *58* (9), 6268–6275.
- (73) First snapshot of a nonpolymeric hydrogelator interacting with its gelling solvents. Kumar, D. K.; Jose, D. A.; Das, A.; Dastidar, P. *Chem. Commun.* **2005**, 4059–4061.
- (74) Baggi, G.; Boiocchi, M.; Fabbri, L.; Mosca, L. Moderate and Advanced Intramolecular Proton Transfer in Urea-Anion Hydrogen-Bonded Complexes. *Chem. - Eur. J.* **2011**, *17*, 9423–9439.
- (75) Naranthatta, M. C.; Das, D.; Tripathy, D.; Sahoo, H. S.; Ramkumar, V.; Chand, D. K. Consequence of Presence and Absence of π -Clouds at Strategic Locations of Designed Binuclear Pd(II) Complexes on Packing: Self-Assembly of Self-Assembly by Intermolecular Locking and Packing. *Cryst. Growth Des.* **2012**, *12*, 6012–6022.
- (76) Custelcean, R.; Moyer, B. A.; Bryantsev, V. S.; Hay, B. P. Anion Coordination in Metal-Organic Frameworks Functionalized with Urea Hydrogen-Bonding Groups. *Cryst. Growth Des.* **2006**, *6*, 555–563.
- (77) Troff, R. W.; Hovorka, R.; Weilandt, T.; Lützen, A.; Cetina, M.; Nieger, M.; Lentz, D.; Rissanen, K.; Schalley, C. A. Equipping metallo-supramolecular macrocycles with functional groups: assemblies of pyridine-substituted urea ligands. *Dalton Trans.* **2012**, *41*, 8410–8420.
- (78) Custelcean, R.; Haverlock, T. J.; Moyer, B. A. Anion Separation by Selective Crystallization of Metal-Organic Frameworks. *Inorg. Chem.* **2006**, *45*, 6446–6452.
- (79) Azhdari Tehrani, A.; Esrafil, L.; Abedi, S.; Morsali, A.; Carlucci, L.; Proserpio, D. M.; Wang, J.; Junk, P. C.; Liu, T. Urea Metal-Organic Frameworks for Nitro-Substituted Compounds Sensing. *Inorg. Chem.* **2017**, *56*, 1446–1454.
- (80) Forgan, R. S.; Marshall, R. J.; Struckmann, M.; Bleine, A. B.; Long, D.-L.; Bernini, M. C.; Fairen-Jimenez, D. Structure-directing factors when introducing hydrogen bond functionality to metal-organic frameworks. *CrystEngComm* **2015**, *17*, 299–306.
- (81) Cametti, M.; Džolić, Z. New frontiers in hybrid materials: noble metal nanoparticles - supramolecular gel systems. *Chem. Commun.* **2014**, *50*, 8273–8286.
- (82) Pastoriza-Santos, I.; Liz-Marzán, L. M. Formation and Stabilization of Silver Nanoparticles through Reduction by N,N-Dimethylformamide. *Langmuir* **1999**, *15*, 948–951.
- (83) Marren, K. Dimethyl sulfoxide: an effective penetration enhancer for topical administration of NSAIDs. *Phys. Sportsmed.* **2011**, *39*, 75–82.